Large extracellular vesicles subsets and contents discrimination: the potential of morpho mechanical approaches at single EV level

Geetika Raizada[1], Benjamin Brunel[1], Joan Guillouzouic[3], Eric Le Ferrec[3], Wilfrid Boireau[1], Eric Lesniewska[2], Céline Elie-Caille[1]

1. Université Marie et Louis Pasteur, UFC, CNRS, Institut FEMTO-ST, F-25000 Besançon, France

2. ICB UMR CNRS 6303, University of Bourgogne, F-21078 Dijon, France

3. EHESP IRSET INSERM UMR_S 1085, University of Rennes, F-35000, Rennes, France

Abstract

Extracellular vesicles are heterogenous lipid bound membranous structures released by different cells, showing a great potential to be used as biomarkers. They have been explored by the researchers for their role in the context of environmental toxicity. When exposed to pollutants like polycyclic aromatic hydrocarbons, they undergo surface modification as well as the change of contents in their cargo. Subpopulations of large EVs (lEVs) have shown to contain both damaged and intact mitochondria which is inexorably linked to oxidative stress conditions. In this study, we aimed to perform morpho-mechanical characterization of the lEVs derived from benzo[a]pyrene (B[a]P) treated endothelial cells. The combination of fluorescence microscopy and atomic force microscopy (AFM) allowed to accurately perform the measurements on the lEVs that contained mitochondria or not. Through morphological study, we obtained the size profile of different EV sub-populations, size of EVs containing mitochondria coming from treated condition (1.8 ± 0.89 µm) and from the control condition (1.63 ± 0.76 µm). Through quantitative measurement of Young's modulus, we found that EVs containing mitochondria from treated condition showed higher stiffness than the control condition ones with the average Young's modulus 3.09 and 1.25 MPa respectively. We also observed the heterogeneity within the single vesicles, having majority of the Young's modulus values ranging from 0.1 up to 30 MPa for the treated condition and 0.1 to 5 MPa for the control condition. Finally, linear discriminant analysis (LDA) was applied as a statistical tool to discriminate EV subpopulations based on maximum diameter, height, and the Young's modulus value distributions. The statistical analysis using LDA confirmed our ability to detect mitochondria within EVs based on morphological and Young's modulus data and demonstrated the potential for discrimination between conditions. Following this, we applied the Random Forest algorithm to the morpho-mechanical data to classify EV subpopulations successfully. This approach enabled us to distinguish EVs containing mitochondria and determine whether these mitochondria-containing EVs originated from control or treated conditions, achieving accuracies of 84% and 76%, respectively. These findings highlight the combined power of morpho-mechanical analysis and machine learning for identifying and discriminating EV subpopulations.

Keywords:
Atomic force microscopy, large extracellular vesicles, mitochondria, Young's modulus, benzo[a]pyrene, machine learning.

Introduction:

Atomic Force Microscopy has been extensively used to study the morphology and mechanical properties of biological materials. It provides the ability to perform the measurements in aqueous solution i.e. physiological conditions with spatiotemporal resolution [1]. AFM utilizes a cantilever which scans the sample and registers the interaction between the tip and the sample in the form of force-distance curves. Through the exploration of these curves, we can obtain viscoelastic properties on the samples [2], [3]. The nanomechanical properties shed light on the physiological state of the biological samples. During recent years, AFM has been employed to study the extracellular vesicles (EVs). EVs are the heterogenous population of lipid bilayer membranous structure that are released from different cells [4]. They are the indicators of different pathologies and carries the information about the originating cells [5]. AFM has been used to identify EV subpopulations and other nanoparticles that could be present in a biological sample. Blood derived EVs were characterized into subpopulations by PeakForce tapping® mode where the distribution of Young's modulus within single vesicle was used to separate EVs subpopulations [6]. *Ridolfi et al.* used the morphological data of EVs obtained by AFM to discriminate different subpopulations. They used contact angle of the individual EVs (stiffness) and size profiles to separate vesicles from the non-vesicular content in the sample [7], [8]. In a different approach, combining AFM with surface plasmon resonance imaging allowed the morphological characteristics of EVs, selectively captured by antibodies grafted onto a surface plasmon resonance-based biochip, to distinguish EV subpopulations based on the selected ligands and varying cell culture conditions [9], [10]. *Leiva-Sabadini et al.* studied the mechanical properties of EVs derived from honey where they measured Young's modulus of small EVs (sEVs), they also used nanoindentation to study the antibacterial effect of sEVs on the membrane of *Streptococcus mutans* [11]. The study of metrology and nanomechanical properties has also been used for diagnostic applications, *Sharma et al*. showed the potential of using morphology of saliva derived exosomes and the expression of CD63 as oral cancer biomarker [12]. In another recent study, AFM was used to obtain nanomechanical signatures of the EVs coming from bone marrow and blood of hematologic cancer patients. They showed a clear difference between the multiple myeloma, lymphoma patients and the healthy donor [13].

In this study, we investigated EVs coming from Human microvascular endothelial cell line (HMEC-1) which are exposed to benzo[a]pyrene (B[a]P). B[a]P is one of the polycyclic aromatic hydrocarbons (PAH) that can be found in diet, smoke, water, etc. When it is exposed to cells, it is known to generate oxidative stress [14] resulting from an influx of reactive oxygen species (ROS) [15] which then causes the processes like lipid peroxidation, DNA damage, etc [16]. The exposure to these toxicants could lead to modification of EV composition, cargo and proteins [17]. There have been several studies which explored EVs as the biomarkers for cytotoxicity and their role in promoting oxidative stress [18], [19]. The rise

in the production of ROS under stress condition could lead to mitochondrial damage as it is intricately link with the metabolism of ROS [20]. The damaged mitochondria can be removed from the cells by different cellular processes like mitosis and mitophagy [21]. It has been shown previously that mesenchymal stem cells derived EVs transferred an intact mitochondrion inside the microvesicles under intracellular oxidative stress [22]. Our experimental model was designed to explore the effect of cytotoxic conditions on the morphological and mechanical properties of the EVs with particular attention paid to possible mitochondria present in EVs at the single EV level. Ultimately, we aimed to use AFM morpho-mechanical data, combined with statistical analysis and machine learning, to identify the presence of mitochondria within large EVs. Finally, the potential of such biophysical investigation for the deciphering of subpopulation of EVs is discussed.

Method:

1. Cell culture and EV isolation

In this study, we employed the HMEC-1 cell line, a human microvascular endothelial cell line, sourced from the Center for Disease Control and Prevention, Atlanta, USA. The cells were cultured in endothelial basal medium MCDB131 (US Biological Life Sciences, Ref E3000-01G) containing 10% decomplemented (56°C, 30 min) fetal bovine serum (FBS, Dutscher, Ref 500105A1A), L-glutamine (Gibco, Ref 25030, 10 mM final), penicillin/streptomycin (Gibco, Ref 15140-122, 100 unit/mL final), gentamycin (Gibco, Ref 15750-037, 500 µg/mL final), epithelial growth factor (EGF, Sigma, Ref E9644, 10 ng/mL final) and Hydrocortisone (Up John, Ref 3400932141159, 1 µg/mL final) in 151.9 cm^2 petri dishes (Corning, Ref 353025). The pH of the medium was adjusted at 7.6 using sodium bicarbonate (Gibco, Ref 25080-060). The medium was replaced every two to three days. Cells underwent weekly passage via trypsinization (trypsin EDTA 0.05%, Gibco, Ref 25300-054). When 90% confluence was achieved, we cultured cells overnight in FBS free medium. Later cells were treated with B[a]P 100 mM (Benzo[a]pyrene, Sigma, Ref B1760) dissolved in DMSO (DMSO, Sigma, Ref D8418), the final concentration of DMSO did not exceed 0.0005% (v/v) (treated condition) and control cell culture were exposed to the same amount of DMSO (control condition).

The method of large EV isolation was previously described by Le Goff et al. [23] which followed the international guidelines for extracellular vesicles isolation [4]. The FBS free medium was centrifuged at 3650 x g for 10 mins at 4°C, this step was done to remove cells and cell debris. Mito Tracker Green FM (MTG) (Thermo Fisher Scientific, USA) at concentration 100 nM was used to label the mitochondria inside the EVs. It was added to the preheated clarified medium (37°C) and was then incubated at 37 °C away in the dark for 45 mins. After the incubation, the clarified medium was ultracentrifuged at 10,000 *g* for 30 mins at 4°C (Optima L-90 K ultracentrifuge and Sw 28.1 Ti rotor or XE-90 ultracentrifuge and Sw 32 Ti rotor), Beckman Coulter, USA). The obtained pellet was washed by centrifuging it in PBS 1X buffer (Gibco, 14190-094) for 30 mins at 4°C. Finally, the pellet was resuspended in 50 µl PBS 1X buffer to be stored at -20°C. Nanoparticle Tracking Analysis (NanoSight NS300, Malvern Instruments, UK) was performed to obtain the concentration of the EVs with the protocol of

5 videos of 60 s (Results: Figure S1). The EVs from the treated condition will be referred to as t-EVs-M (treated EVs containing mitochondria) and t-EVs (treated EVs without mitochondria). For the control condition, they will be referred to as c-EVs-M (control EVs containing mitochondria) and c-EVs (control EVs without mitochondria).

2. Substrate preparation and Sample deposition

All the morpho mechanical measurements were performed on freshly cleaved mica as the substrate. Since mica inherently have negative charge, we introduced mica sheets with divalent positive ions right after cleaving. The mica sheets (*Agar Scientific, Ref: AGG250*) were first cleaved with a scotch tape, then we quickly added 50 µl HEPES 10mM (Sigma-Aldrich, H3375-100G) + $CaCl_2$ 5 mM (Sigma-Aldrich, 223506-500G) buffer solution onto the cleaved surface. After incubating the sheets for approximately 10 mins at the room temperature. We added 5 µl sample solution containing EVs and 25 µl of the solution was mixed gently at three different places. This step allowed us to distribute the EVs on the mica surface as uniformly as possible and to avoid forming exceptionally large aggregates. Then we left the mica sheet with EV sample to incubate for another 10 – 15 mins. Afterwards, we gently removed 25 µl from the buffer droplet to eliminate any floating objects that were not adsorbed on the mica surface. We then added 25 µl buffer to further imaging under AFM.

3. Optical calibration between fluorescence and atomic force microscopy

The prepared mica sheet was observed under fluorescence microscope using 40x objective at the excitation wavelength of 480 nm to observe the EVs containing mitochondria. The laser was aligned on the top of the AFM tip and the optimal SUM signal was obtained. Once the tip has approached the surface, we retracted the tip up to 20 µm which allowed us still to view the tip while performing optical calibration. AFM apparatus (*Bruker Nanowizard®4 Bioscience* system) allowed the optical calibration by using the feature DirectOverlay™ which allowed us to determine whether the scanned area contained EV with mitochondria or not. The calibration is usually done by acquiring the optical image of AFM tip at 25 or more different positions. The coordinates of tip at each position are automatically determined by AFM closed loop scanning system. These coordinates will help in accurately overlaying AFM image on the top of the fluorescence image. After the calibration step, we took a snapshot image to be used as a guide for scanning. After obtaining one or two AFM images, shifted optical image can be used to further adjust the alignment between the optical and AFM images. This calibration allowed to precisely identify whether the EV contained mitochondria or not.

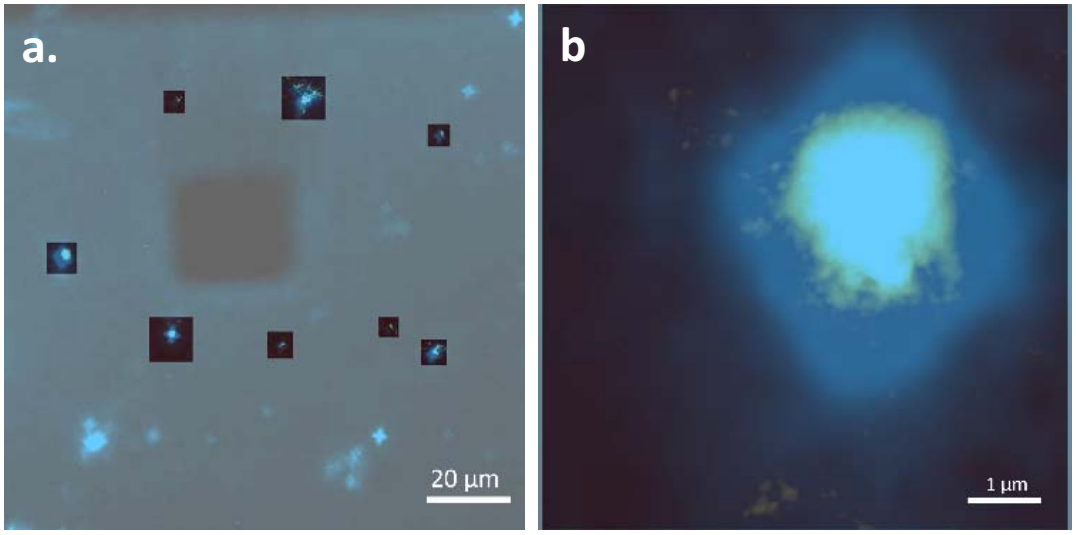

Figure 1. EVs derived from HMEC cells, adsorbed on mica, by AFM coupled with fluorescence microscope. Overlaid AFM images on the top of fluorescence image obtained using 40x objective. a) Fluorescence image containing several AFM images; b) Focused AFM image of EV containing mitochondria with the fluorescent spot in the background.

4. Quantitative Imaging (QI) measurements

QP-BIO-AC cantilever from *Nanosensors* was used for all the QI measurements. These cantilevers with the tip radius 10 nm have low spring constant (0.06 – 0.3 N/m) which makes them suitable for scanning biological objects. The imaging was performed in liquid to maintain the physiological conditions for the EVs in the QI mode. In this mode, the force-distance curves (Fig 2) at each pixel are recorded which would enable us to calculate Young's modulus of the objects scanned. The imaging was performed with the resolution of 256 x 256 pixels at the constant tip velocity. The low setpoint values were used to ensure that we do not rupture the EV membrane while keeping the indentation at about 1-2 %. The setpoint value was kept between 0.3 – 0.5 nN except for the cases where high setpoint was required. The area of scanning was dependent on the region selected on the fluorescence image usually between 2 x 2 to 5 x 5 μm^2 but not exceeding 10 x 10 μm^2.

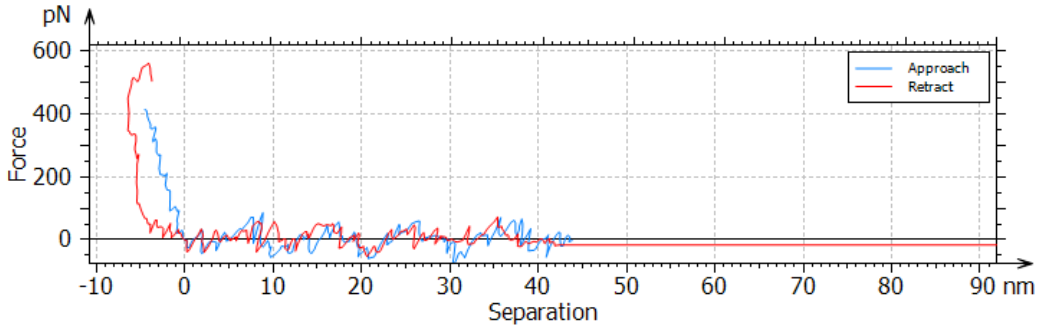

Figure 2. Example of raw force-distance curve registered on a large EV obtained using QI mode in liquid. Tip used: QP-BIO-AC; Spring constant: 0.06- 0.3 N/m; Tip radius: 10 nm.

5. Image treatment, data extraction and indentation model

All the images and QI data were treated using Mountain's SPIP 9 software. To obtain the size profile of the EVs, particle analysis was performed using a height threshold of 8.5 nm, which helped exclude free proteins and other elements that might have been adsorbed on the substrate from the sample solution, ensuring they were not considered during analysis. We first extracted force-distance curves at the random points on EVs as shown in Fig 3 while avoiding all the points that are at the edge of the EV; then *Savitzky-Golay* filter was applied for noise filtering. Afterwards, we performed the baseline correction by subtracting 1 polynomial degree. The obtained curves were then calibrated by applying the values of photodiode sensitivity (the ratio of the deflection of the tip and the change in voltage output) and cantilever's spring constant (k); this step allowed the measurement of the forces between the tip and the surface. To calculate the elastic modulus (Young's modulus), we applied *Derjaguin–Muller–Toropov* (DMT) model [24] keeping Poisson's ratio as 0.3 for the analysis.

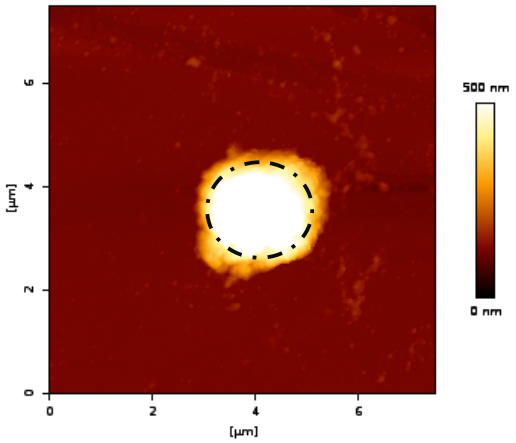

Figure 3. AFM (height channel) image showing one large EV; the region within the dotted line shows where we extracted the force-distance curves from random points (avoiding the edge of the vesicles)

6. Statistical Analysis

Linear Discriminant Analysis (LDA) was performed on the Young's modulus distribution (proportion of values in >1, 1-5, and 5 MPa), maximum height, and the maximum diameter to see the discrimination between different EV subpopulations measured. Analysis of variance (ANOVA) was performed on the LD1 and LD2 scores obtained, it was done to verify if there is a significant difference present between different populations or not. We applied the supervised Random Forest algorithm to distinguish EV subpopulations based on morpho-mechanical data, using the same assumptions as in the LDA analysis. The model's performance was evaluated using Leave-One-Out Cross-Validation (LOOCV), ensuring unbiased discrimination and robust evaluation on this dataset. We used the 'scikit-learn' and 'SciPy' python libraries for LDA, random forest and ANOVA.

Results and discussion:

1. Morphological study of different conditions

The nanoscopic resolution offered by AFM has enabled us to closely examine the morphology of EVs derived from two different culture conditions i.e., control and treated. In our work, we concentrated primarily on the analysis of large EVs, those with diameters exceeding 200 nm. It must be noted that the different substrates and sample preparation techniques will influence the shapes of the EVs. For our experiments, we utilized mica sheets treated with bivalent positive ions, which provide a remarkably flat surface having the average roughness Ra of 914.4 pm. The positive charge of the substrate surface facilitated the adsorption of the inherently negatively charged EVs without any additional selective process [25]. In most AFM images, we predominantly observed EVs with spherical geometries (as shown in figures 4a, b, c, and d).

Notably, under the treated condition, we detected small vesicle-like structures clustering around and connected through fibres with lEVs (figure 4e). The lEVs in this structure ranged from 0.3 to 1.3 µm in size and were observed to contain mitochondria, a finding confirmed by fluorescence imaging (Figure S2). In another instance as shown in figure 4f, we observed a bead-like structure. These bead-like formations displayed heights ranging from 20 nm to approximately 50 nm, with profile sections closely resembling those of small EVs. These observations led us to hypothesize that these structures could correspond to migrasomes containing mitochondria [26], [27], with the smaller vesicle clusters possibly representing retractosomes [28].

Using Atomic Force Microscopy (AFM), we were able to conduct detailed size profiling of the EVs under study. Employing Mountain's SPIP software for the analysis, we assessed the EV size based on their maximum diameter and maximum height, as depicted in figure 5a and b. Figure 5a illustrates the distribution of EV sizes in terms of their maximum diameter, highlighting the presence of distinct EV subpopulations in both experimental conditions. The diameters of the EVs ranged significantly; reaching up to 5 µm. EVs devoid of mitochondria tend to be smaller on average than those that contain mitochondria. The mean maximum diameter calculated for c-EVs was 0.55 ± 0.37 µm and 0.47 ± 0.45 µm for t-EVs. From the box plot in figure 5b, it is evident that the t-EVs-M didn't exhibit significantly different maximum diameter from the c-EVs-M. Specifically, the average maximum diameter for the t-EVs-M is 1.8 ± 0.89 µm, whereas the c-EVs-M have an average maximum diameter of 1.63 ± 0.76 µm. After performing ANOVA on the maximum diameter of the lEVs with mitochondria (t-EVs-M and c-EVs-M) from the both conditions, we obtained the p-value of 0.099, which indicates the differences between the size of lEVs from the two conditions was not statistically significant. This observation aligns with the study done by *Le Goff et al*., they also didn't observe significant change in the size of lEVs coming from B[a]P treated condition [23]. Additionally, we also extracted the height of the EV subtypes (figure 5b) where we observed c-EVs-M were taller than t-EVs-M with the mean obtained was 1241 ± 1510 nm and 649 ± 491 nm respectively. Since we are using positively charged surface and the EVs are negatively charged, the observed height differences might be attributed to structural

modification caused by B[a]P treatment. This data highlights the differences in size distributions among various EV subtypes under different conditions.

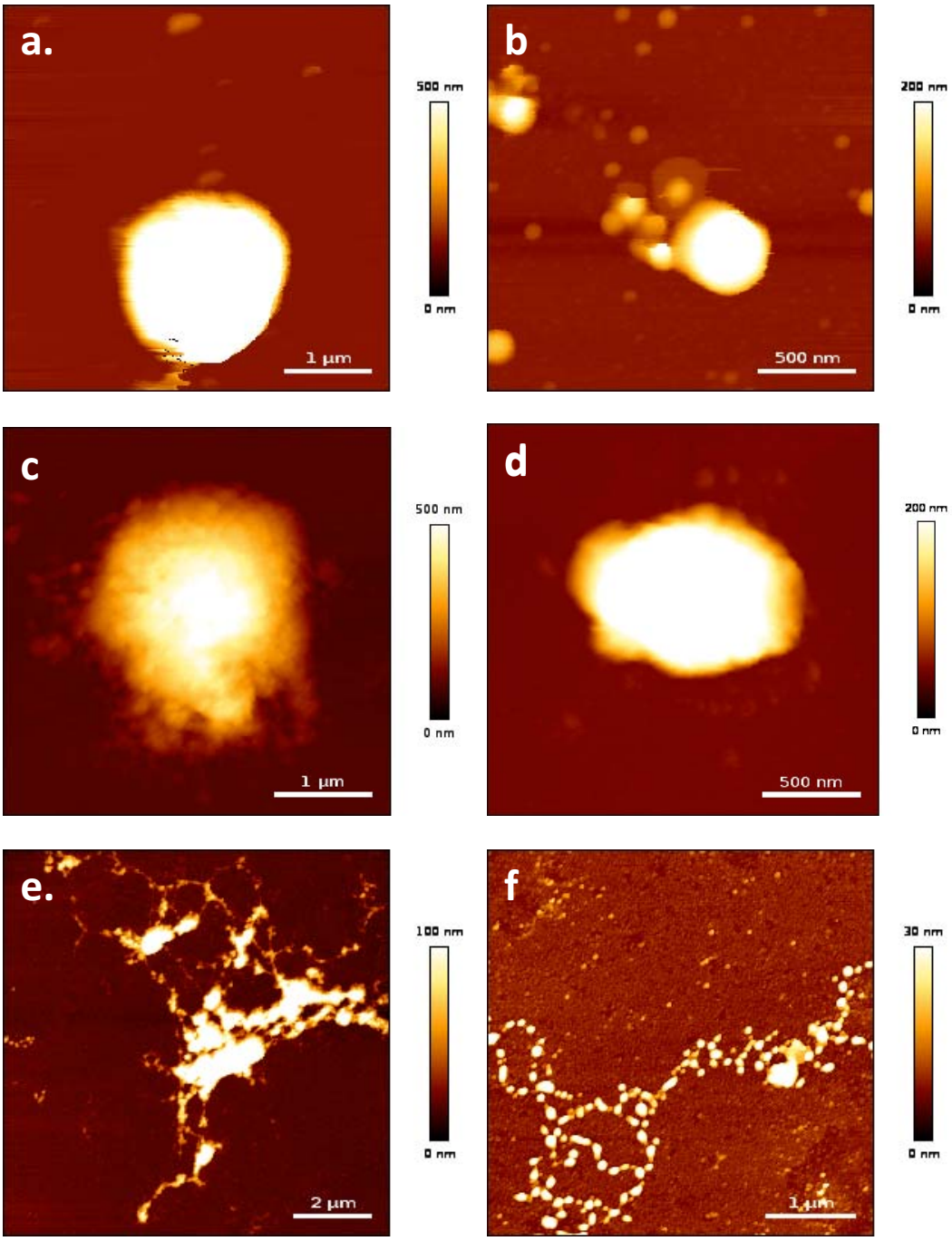

Figure 4. Morphological structure observed by AFM. a and b: lEV from control condition, c and d: lEV from treated condition, e and f: potential structure that could represent migrasomes and rectractosomes from treated condition respectively.

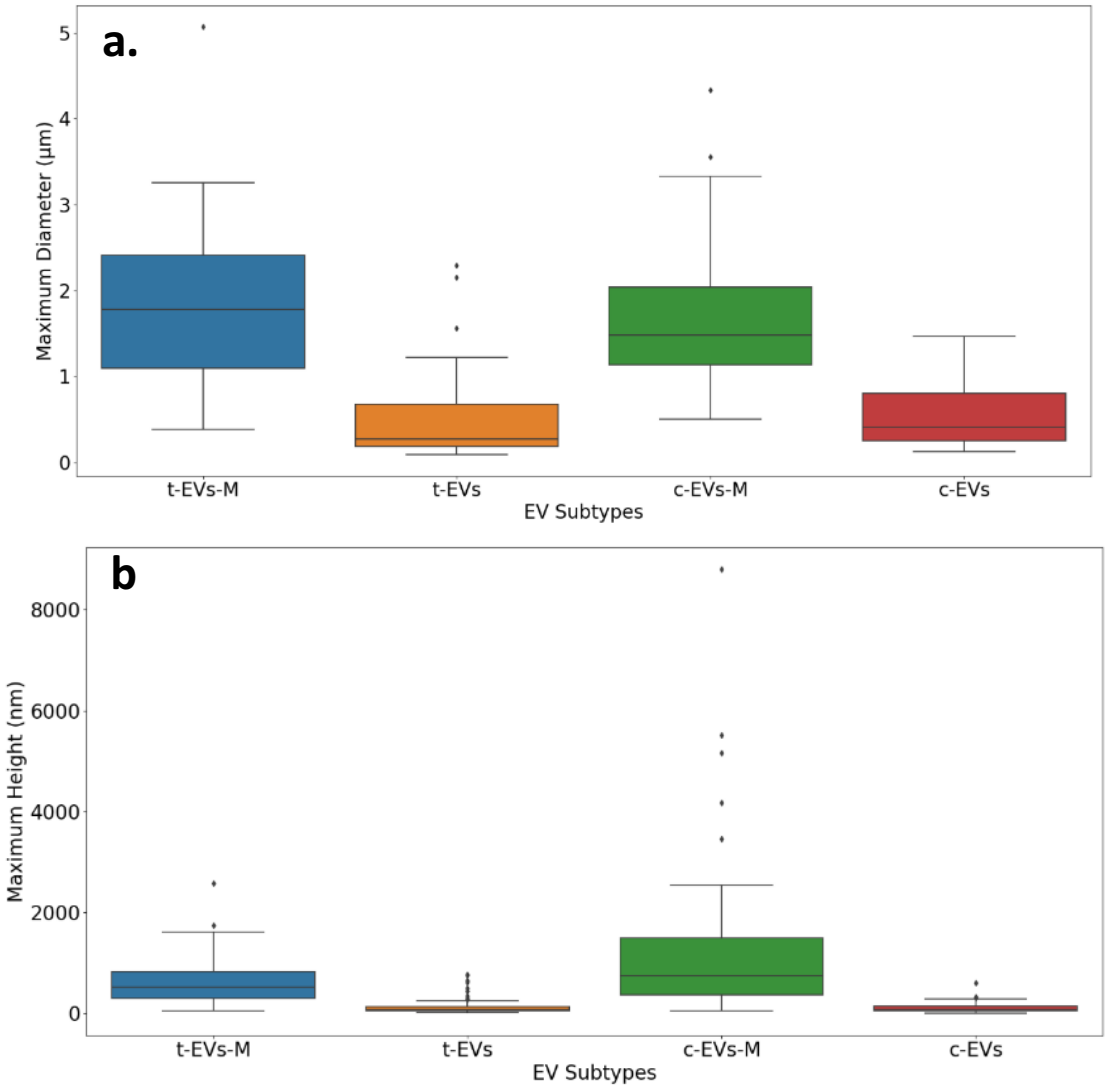

Figure 5. Size distribution of EV subtypes. a. box plot of maximum diameter and b. box plot of maximum height. For the size distribution, we measured 51 t-EVs-M, 69 t-EVs, 59 c-EVs-M and 53 c-EVs.

2. Nanomechanical discrimination

The employment of QI mode in AFM allowed us to investigate the mechanical properties of EVs. We utilized the geometry of the AFM tips in the indentation model (DMT) to generate Young's modulus maps as depicted in figure 6. The Young's modulus maps provided us with the preliminary understanding of the elasticity of the various EV subpopulations present in both samples. Simply based on the young's modulus map, we can observe that c-EVs-M (figure 6a) tended to be softer than the ones from the t-EVs-M (figure 6c). The EVs without mitochondria from both conditions (figure 6a, b, and d) tended to exhibit comparable elasticity. The difference in the elasticity of EVs from different conditions could be due to the modification of surface and cargo. In the oxidative stress conditions, EVs have shown to have both beneficial and deleterious effect of ROS metabolism [29]. In both cases, EVs go through

the modification of the content either by carrying antioxidant machinery or due to the processes like lipid peroxidation which can induce the changes in the membrane fluidity [30].

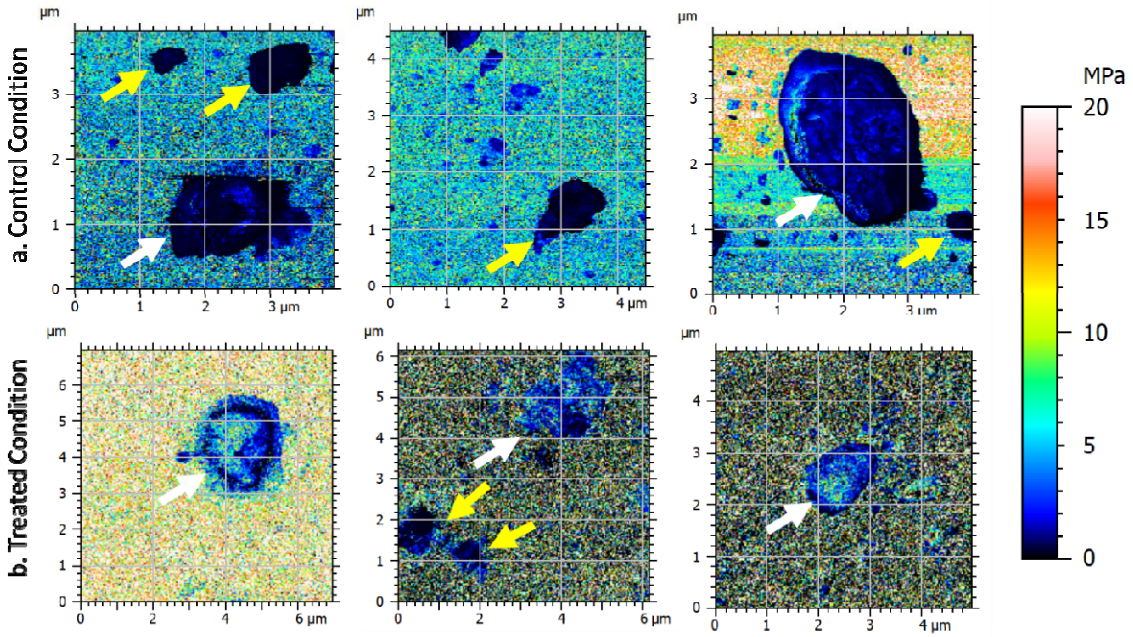

Figure 6. Young's modulus maps generated after applying DMT indentation model. a. from control condition, b. from treated. The white arrow indicated the EVs containing mitochondria and yellow arrows indicating EVs without mitochondria.

Following a qualitative discrimination of the EVs, we proceeded to extract the force-distance curves from individual EVs. This step was essential to establish the distribution profile of Young's modulus values across single EVs. By analysing these curves, we aimed to gain a deeper understanding of the mechanical properties and variability of the EVs at a single-vesicle level. For each individual vesicles, we extracted several values of Young's modulus, which were categorized into three distinct ranges: < 1 MPa, 1-5 MPa, and > 5 MPa (Note that the sum of the 3 proportions is always 100 % which explains why all the dots in fig 7 are inside a plane). This categorization allowed us to visualize systematically the distribution of Young's modulus of individual EVs. To further cluster the EV subpopulations according to their elasticity, we used the 3D plot, which effectively illustrated the distribution and frequency of the Young's modulus values across the different categories (Figure 7a). Figure 7a highlights the distinct elasticity profiles among various EV subpopulations. t-EVs-M (represented by blue dots) exhibited higher stiffness as it has the higher proportion of values exceeding 5 MPa. In contrast, c-EVs-M showed slightly less stiffness as it contained less proportion of values surpassing 5 MPa. Additionally, the Young's modulus distribution profile of EVs without mitochondria from both conditions (t-EVs and c-EVs) demonstrated the tendency to have Young's modulus value less than 5 MPa (orange dots for treated condition and red for the control condition). Through these observations, the distinct clusters of EV subpopulations, differentiated by their elasticity, can be visualized in the 3D plot the different clouds of EV subpopulation according to their elasticity. In the Figure 7b, the box plot shows

the overall distribution of average Young's modulus values of EV subpopulation. t-EVs-M showed the wide distribution of Young's modulus values compared to the other subpopulations. This differentiation suggests that the presence of mitochondria significantly influence the elasticity of EVs, the treatment had the notable effect on the elasticity of the EVs with mitochondria. The average Young's modulus obtained for EVs containing mitochondria was 3.09 and 1.25 for t-EVs-M and c-EVs-M respectively. While the EVs without mitochondria were overall softer with the average Young's modulus value 1.03 and 0.96 MPa for t-EVs and c-EVs respectively.

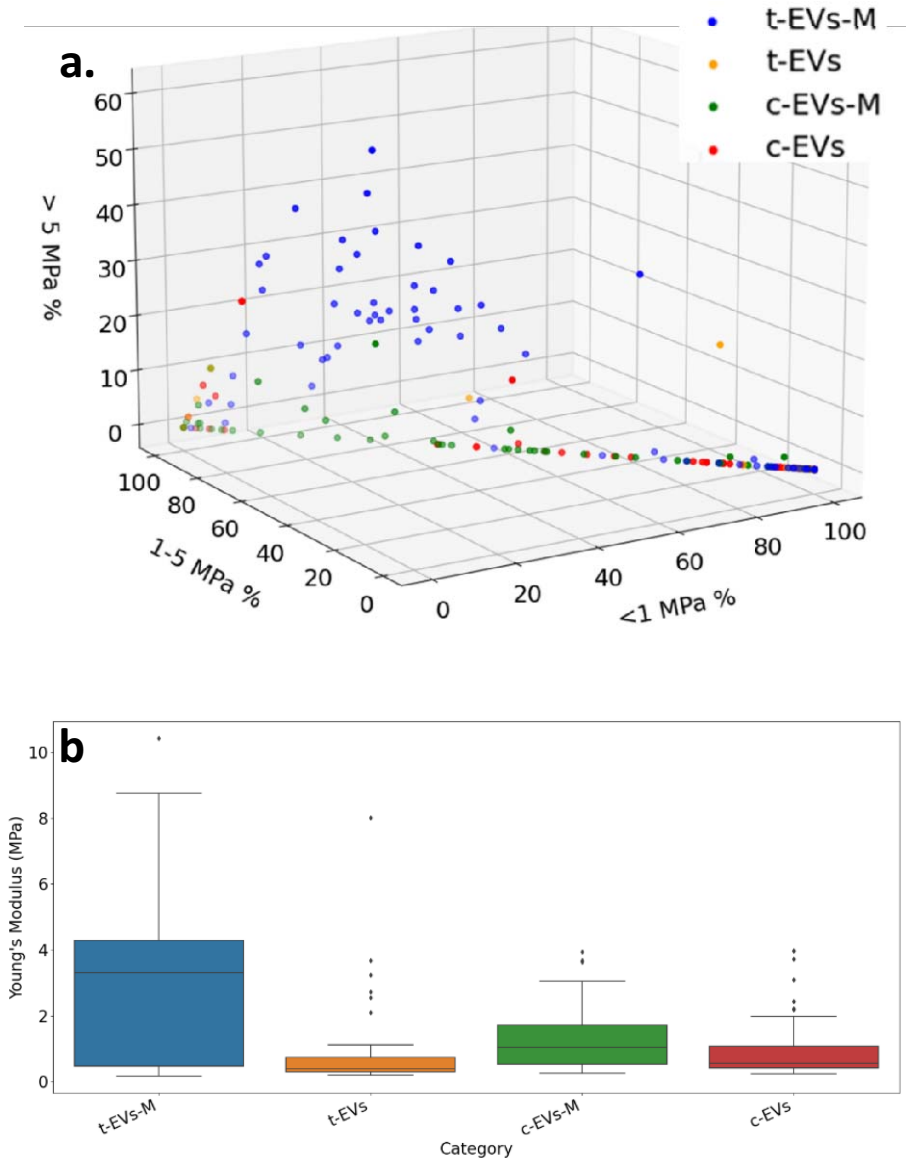

Figure 7. Young's Modulus distribution of EVs derived from cells, in both conditions in liquid. a. 3D plot generated by MATLAB: categorized distribution of Young's modulus values on single EV. Here each dot represents one EV. b. Box plot of all the average Young's modulus obtained for different EV subpopulations. For

this analysis, we measured 102 EVs coming from the treated condition and 114 EVs coming from the control condition. Blue: t-EVs-M; Orange: t-EVs; Green: c-EVs-M and Red: c-EVs.

The resulting Young's modulus distribution profile helped in observing the mechanical heterogeneity within the population of EVs. Bairamukov et al. also observed this heterogeneity within individual vesicles and in the lEVs subpopulation derived from blood plasma. Using AFM, they measured a Young's modulus of 22.48 MPa [6]. In another study, the Young's modulus of the honey derived EVs (sEVs) was determined to be in between ~3–165 MPa [11], this distribution suggests the presence of several EVs subpopulation present in the sample. Various cell sources and their physiological states affect the mechanical characteristics of extracellular vesicles. As was observed by Feng et al., they studied the nanomechanical signature of the EVs originating from blood and bone marrow of healthy donors and different cancer type patients. Not only did they measure the difference between the EVs coming from different sources from one patient, but also different Young's modulus was observed from healthy donor and cancer patients (Myeloma and Lymphoma) [13].

Another important aspect when calculating the Young's modulus values is to consider the indentation model applied. Normally the indentation model is chosen according to the shape of the AFM tip utilized, the adhesion forces between tip and the samples. We applied DMT indentation model, based on hertz theory to calculate the Young's modulus, this model was suitable for spherical shaped AFM tip used where the adhesion force between the tip and the sample was very small [1]. However, this model works on the assumption that the mechanical properties of EV are homogenous across the surface [31], which is not the accurate representation of EVs as can be noticed through our findings. Other models like thin shell and Canham Helfrich theory based models have been used for EVs, in these models the mechanical properties are dependent on the size of the EVs [32], [33], [34]. Each model is based on the assumptions that might not necessarily be applicable for the EVs, but all the model highlights the heterogeneity among the EV populations. Recently it has been becoming prevalent to focus on statistical and machine learning methods that can provide faster and accurate analysis [35]. These methods have also shown the potential to identify the correlations within large datasets and identify the crucial features in the data [36]. The machine learning algorithms has already been used to classify cell surfaces of biological cells [37] and there is a great potential to use the same approach to classify and characterize EV subpopulations [38].

3. Statistical analysis

LDA was applied to visualize the discrimination between different EV subpopulation where we used Young's modulus distribution, height, and the maximum diameter as the features for each EV. LD1 and LD2 were linear discriminants derived from the LDA transformation, there discriminants helped in the maximizing the variance between different population while reducing the variance within each population.

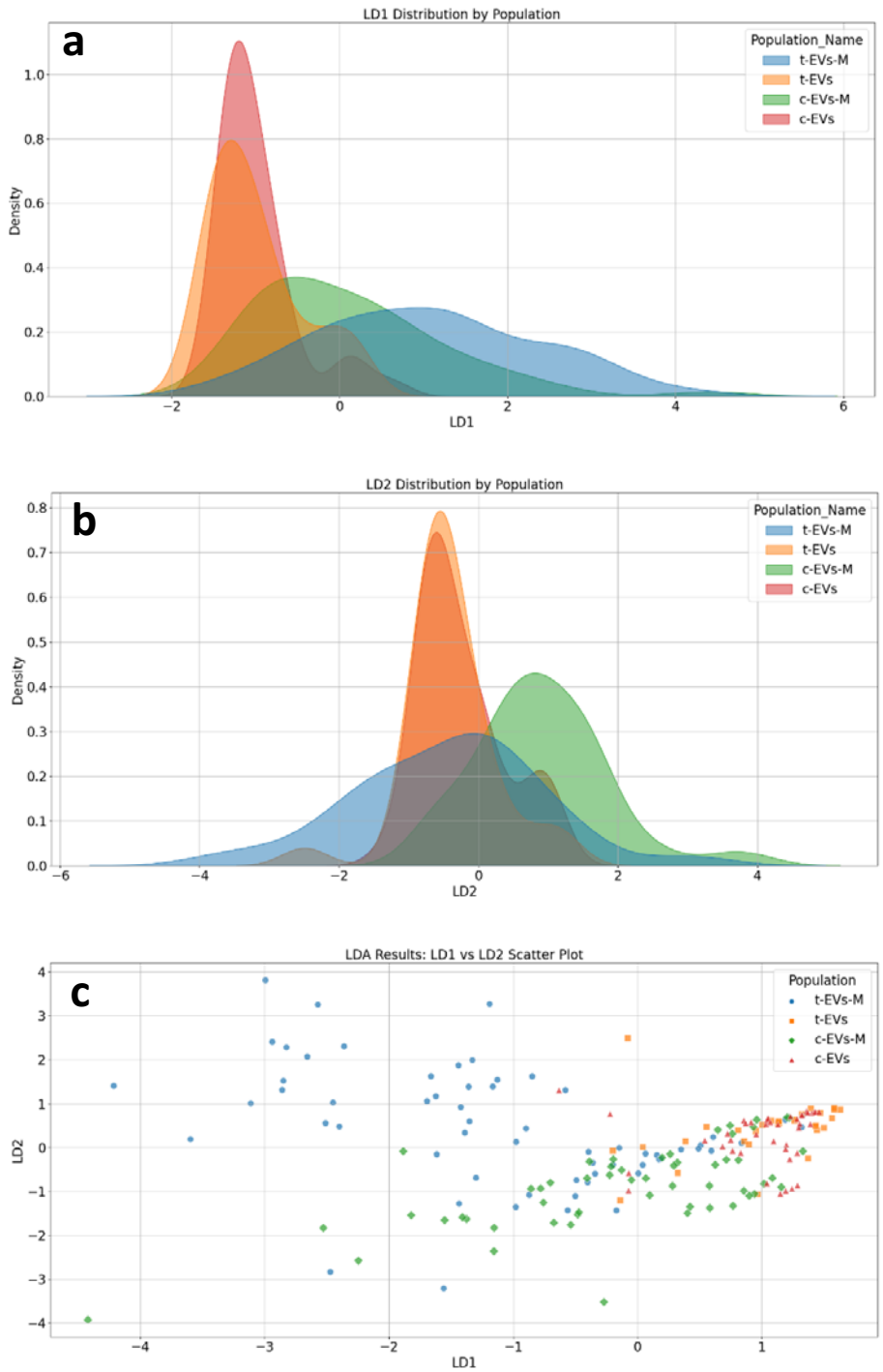

Figure 8. LDA analysis for EV discrimination. Here a and b are distribution curves based on LD1 and LD2 respectively. c is the scatter plot between LD1 and LD2 score where each point in the plot represents an individual EV. Blue: t-EVs-M; Orange: t-EVs; Green: c-EVs-M and Red: c-EVs.

In the Figure 8, the first curve is the distribution of each population according to the LD1. Here, we can clearly observe the separation of EVs with mitochondria from EVs without mitochondria. Hence, we decided to perform ANOVA on LD1 scores of the EV with

mitochondria (t-EVs-M and c-EVs-M) and EV without mitochondria (tEVs and cEVs) with the assumption that with LD1 scores, we can identify the EVs containing mitochondria. We obtained p-value 9.47 10^{-20}, indicating that the difference in LD1 is significant between the combined population of EVs containing or not mitochondria. Another hypothesis tested with ANOVA was that control, and treated conditions could be discriminated for EVs containing mitochondria. We used LD2 scores of t-EVs-M and c-EVs-M, we obtained a p-value 1.1 10^{-8}. These results confirm that with LDA on three variables, we can differentiate between the populations while ANOVA further confirms the significance of the differences observed.

After confirming the reliability of morpho-mechanic data (Young's modulus, height, and the maximum diameter) to discriminate different EV subpopulations, we applied the same assumptions to the Random Forest algorithm. This algorithm creates multiple decision trees using random subsets of data and features, combining results to improve accuracy and reduce overfitting. We tested this model using LOOCV where n-1 data points are used for training, and the remaining single data point is used for testing, repeating this process for all data points. The confusion matrices (Figure 9) present the results obtained using this prediction model. The model achieved an accuracy of 84.21% in identifying EVs containing mitochondria from others (Assumption 1). Additionally, it achieved 76.19% accuracy in distinguishing c-EVs-M from t-EVs-M (Assumption 2).

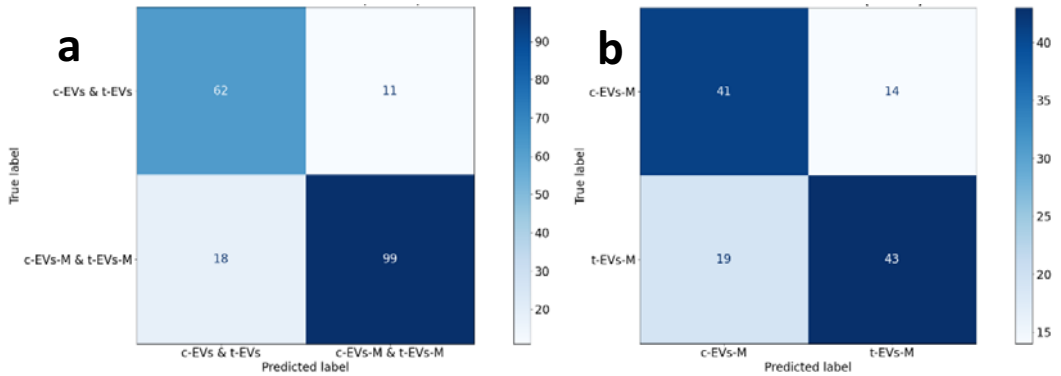

Figure 9. Confusion matrix of the prediction of EV subpopulations. a. Prediction results for identifying EVs containing mitochondria. b. Prediction results for distinguishing between c-EVs-M and t-EVs-M.

Conclusion:

This study explored a way to discriminate EVs originating from HMEC- cells exposed to B[a]P or not through morpho mechanical properties. The discrimination was based on the measurements obtained at single vesicle level. The elastic modulus of EVs offered insights into both their physiological state and the culture condition of the parent cells. By examining the mechanical properties of the EVs, we could determine their membrane rigidity and differentiate different subpopulations based on their nanomechanical properties. Using a combination of fluorescence microscopy and atomic force microscopy, we were able to measure accurately the elasticity of EVs containing mitochondria or not. Our findings

revealed that EVs containing mitochondria from B[a]P-treated cells were discernibly stiffer than those from control cells, with average Young's modulus values of 3.09 MPa and 1.03 MPa, respectively. Through statistical methods such as LDA and ANOVA, we demonstrated the ability to discriminate between EVs containing mitochondria and those without, showing a significant difference in morpho-mechanical properties (p-value = 9.5×10^{-20}). Additionally, we confirmed the possibility of distinguishing the source of mitochondria-containing EVs (control vs. treated) with a p-value = 1.1×10^{-8}. The results from the Random Forest model further validate the effectiveness of this approach in accurately identifying and classifying EV subpopulations. The high accuracy achieved emphasize the potential of morpho-mechanical data for robust classification, particularly in identifying mitochondria-containing EVs and differentiating their sources. This combined approach can be easily applied to study other samples, offering a straightforward and accessible technique to follow. Future improvements as immuno-enrichment on the chip can further aid in selecting specific EV subpopulations. We emphasize that such study could be envisioned as a nanoanalytical method to assess the impact of various toxicological pollutants on EVs and may also serve as a diagnostic tool for a wide range of medical applications.

Acknowledgments and fundings:

This work has been funded by the EIPHI Graduate School (contract ANR-17-EURE-0002) and Bourgogne-Franche-Comté Region. This work was supported by the French National Agency for Research (ANR; ENDOMITOPAH project: R23137NN). The authors wish to thank the laboratory staff of the Clinical-Innovation Proteomic Platform (CLIPP) and Nano2BIO team at FEMTO-ST Institute for fruitful discussion and technical/instrumental supports.

References:

[1] M. Krieg *et al.*, « Atomic force microscopy-based mechanobiology », *Nat. Rev. Phys.*, vol. 1, n° 1, p. 41–57, nov. 2018, doi: 10.1038/s42254-018-0001-7.

[2] F. M. Hecht, J. Rheinlaender, N. Schierbaum, W. H. Goldmann, B. Fabry, et T. E. Schäffer, « Imaging viscoelastic properties of live cells by AFM: power-law rheology on the nanoscale », *Soft Matter*, vol. 11, n° 23, p. 4584–4591, 2015, doi: 10.1039/C4SM02718C.

[3] A. Raman *et al.*, « Mapping nanomechanical properties of live cells using multi-harmonic atomic force microscopy », *Nat. Nanotechnol.*, vol. 6, n° 12, p. 809–814, déc. 2011, doi: 10.1038/nnano.2011.186.

[4] J. A. Welsh *et al.*, « Minimal information for studies of extracellular vesicles (MISEV2023): From basic to advanced approaches », *J. Extracell. Vesicles*, vol. 13, n° 2, p. e12404, févr. 2024, doi: 10.1002/jev2.12404.

[5] M. Simons et G. Raposo, « Exosomes--vesicular carriers for intercellular communication », *Curr. Opin. Cell Biol.*, vol. 21, n° 4, p. 575–581, août 2009, doi: 10.1016/j.ceb.2009.03.007.

[6] V. Yu. Bairamukov *et al.*, « Nanomechanical characterization of exosomes and concomitant nanoparticles from blood plasma by PeakForce AFM in liquid », *Biochim. Biophys. Acta BBA - Gen. Subj.*, vol. 1866, n° 7, p. 130139, juill. 2022, doi: 10.1016/j.bbagen.2022.130139.

[7] A. Ridolfi *et al.*, « AFM-Based High-Throughput Nanomechanical Screening of Single Extracellular Vesicles », *Anal. Chem.*, vol. 92, n° 15, p. 10274–10282, août 2020, doi: 10.1021/acs.analchem.9b05716.

[8] A. Ridolfi *et al.*, « Particle profiling of EV-lipoprotein mixtures by AFM nanomechanical imaging », *J. Extracell. Vesicles*, vol. 12, n° 10, p. e12349, oct. 2023, doi: 10.1002/jev2.12349.

[9] G. Raizada *et al.*, « Multimodal Analytical Platform on a Multiplexed Surface Plasmon Resonance Imaging Chip for the Analysis of Extracellular Vesicle Subsets », *J. Vis. Exp. JoVE*, n° 193, mars 2023, doi: 10.3791/64210.

[10] G. Raizada *et al.*, « NanoBioAnalytical (NBA) Platform to Decipher Extracellular Vesicles Secreted by Microvascular Endothelial Cells Under Benzo[a]pyrene Exposure », *Preprints*, janv. 2025, doi: 10.20944/preprints202501.0599.v1.

[11] C. Leiva-Sabadini, S. Alvarez, N. P. Barrera, C. M. A. P. Schuh, et S. Aguayo, « Antibacterial Effect of Honey-Derived Exosomes Containing Antimicrobial Peptides Against Oral Streptococci », *Int. J. Nanomedicine*, vol. 16, p. 4891–4900, 2021, doi: 10.2147/IJN.S315040.

[12] S. Sharma, B. M. Gillespie, V. Palanisamy, et J. K. Gimzewski, « Quantitative nanostructural and single-molecule force spectroscopy biomolecular analysis of human-saliva-derived exosomes », *Langmuir ACS J. Surf. Colloids*, vol. 27, n° 23, p. 14394–14400, déc. 2011, doi: 10.1021/la2038763.

[13] Y. Feng, M. Liu, X. Li, M. Li, X. Xing, et L. Liu, « Nanomechanical Signatures of Extracellular Vesicles from Hematologic Cancer Patients Unraveled by Atomic Force Microscopy for Liquid Biopsy », *Nano Lett.*, vol. 23, n° 4, p. 1591–1599, févr. 2023, doi: 10.1021/acs.nanolett.3c00093.

[14] J. B. Hoffman, M. C. Petriello, et B. Hennig, « Impact of nutrition on pollutant toxicity: an update with new insights into epigenetic regulation », *Rev. Environ. Health*, vol. 32, n° 1–2, p. 65–72, mars 2017, doi: 10.1515/reveh-2016-0041.

[15] G. Pizzino *et al.*, « Oxidative Stress: Harms and Benefits for Human Health », *Oxid. Med. Cell. Longev.*, vol. 2017, p. 8416763, 2017, doi: 10.1155/2017/8416763.

[16] Q. Deng *et al.*, « Polycyclic aromatic hydrocarbons-associated microRNAs and their interactions with the environment: influences on oxidative DNA damage and lipid peroxidation in coke oven workers », *Environ. Sci. Technol.*, vol. 48, n° 7, p. 4120–4128, avr. 2014, doi: 10.1021/es4055516.

[17] C. M. Eckhardt, A. A. Baccarelli, et H. Wu, « Environmental Exposures and Extracellular Vesicles: Indicators of Systemic Effects and Human Disease », *Curr. Environ. Health Rep.*, vol. 9, n° 3, p. 465–476, sept. 2022, doi: 10.1007/s40572-022-00357-5.

[18] N. Van Meteren *et al.*, « Extracellular vesicles released by polycyclic aromatic hydrocarbons-treated hepatocytes trigger oxidative stress in recipient hepatocytes by delivering iron », *Free Radic. Biol. Med.*, vol. 160, p. 246–262, nov. 2020, doi: 10.1016/j.freeradbiomed.2020.08.001.

[19] N. Van Meteren *et al.*, « Polycyclic Aromatic Hydrocarbons Can Trigger Hepatocyte Release of Extracellular Vesicles by Various Mechanisms of Action Depending on Their Affinity for the Aryl Hydrocarbon Receptor », *Toxicol. Sci.*, vol. 171, n° 2, p. 443–462, oct. 2019, doi: 10.1093/toxsci/kfz157.

[20] C. Guo, L. Sun, X. Chen, et D. Zhang, « Oxidative stress, mitochondrial damage and neurodegenerative diseases », *Neural Regen. Res.*, vol. 8, n° 21, p. 2003–2014, juill. 2013, doi: 10.3969/j.issn.1673-5374.2013.21.009.

[21] P. Venditti, L. Di Stefano, et S. Di Meo, « Mitochondrial metabolism of reactive oxygen species », *Mitochondrion*, vol. 13, n° 2, p. 71–82, mars 2013, doi: 10.1016/j.mito.2013.01.008.
[22] D. G. Phinney *et al.*, « Mesenchymal stem cells use extracellular vesicles to outsource mitophagy and shuttle microRNAs », *Nat. Commun.*, vol. 6, n° 1, p. 8472, oct. 2015, doi: 10.1038/ncomms9472.
[23] M. Le Goff *et al.*, « PAHs increase the production of extracellular vesicles both in vitro in endothelial cells and in vivo in urines from rats », *Environ. Pollut.*, vol. 255, p. 113171, déc. 2019, doi: 10.1016/j.envpol.2019.113171.
[24] B. V. Derjaguin, V. M. Muller, et Yu. P. Toporov, « Effect of contact deformations on the adhesion of particles », *J. Colloid Interface Sci.*, vol. 53, n° 2, p. 314–326, nov. 1975, doi: 10.1016/0021-9797(75)90018-1.
[25] C. Elie-Caille, F. Severin, J. Helenius, J. Howard, D. J. Muller, et A. A. Hyman, « Straight GDP-Tubulin Protofilaments Form in the Presence of Taxol », *Curr. Biol.*, vol. 17, n° 20, p. 1765–1770, oct. 2007, doi: 10.1016/j.cub.2007.08.063.
[26] X. Tan, S. He, F. Wang, L. Li, et W. Wang, « Migrasome, a novel organelle, differs from exosomes », *Biochem. Biophys. Rep.*, vol. 35, p. 101500, sept. 2023, doi: 10.1016/j.bbrep.2023.101500.
[27] H. Jiao *et al.*, « Mitocytosis, a migrasome-mediated mitochondrial quality-control process », *Cell*, vol. 184, n° 11, p. 2896-2910.e13, mai 2021, doi: 10.1016/j.cell.2021.04.027.
[28] Y. Wang *et al.*, « Retractosomes: small extracellular vesicles generated from broken-off retraction fibers », *Cell Res.*, vol. 32, n° 10, p. 953–956, oct. 2022, doi: 10.1038/s41422-022-00666-2.
[29] G. Bodega, M. Alique, L. Puebla, J. Carracedo, et R. M. Ramírez, « Microvesicles: ROS scavengers and ROS producers », *J. Extracell. Vesicles*, vol. 8, n° 1, p. 1626654, 2019, doi: 10.1080/20013078.2019.1626654.
[30] E. Chiaradia *et al.*, « Extracellular Vesicles under Oxidative Stress Conditions: Biological Properties and Physiological Roles », *Cells*, vol. 10, n° 7, p. 1763, juill. 2021, doi: 10.3390/cells10071763.
[31] M. LeClaire, J. Gimzewski, et S. Sharma, « A review of the biomechanical properties of single extracellular vesicles », *Nano Sel.*, vol. 2, n° 1, p. 1–15, janv. 2021, doi: 10.1002/nano.202000129.
[32] B. Whitehead *et al.*, « Tumour exosomes display differential mechanical and complement activation properties dependent on malignant state: implications in endothelial leakiness », *J. Extracell. Vesicles*, vol. 4, p. 29685, 2015, doi: 10.3402/jev.v4.29685.
[33] F. Royo *et al.*, « Differences in the metabolite composition and mechanical properties of extracellular vesicles secreted by hepatic cellular models », *J. Extracell. Vesicles*, vol. 8, n° 1, p. 1575678, 2019, doi: 10.1080/20013078.2019.1575678.
[34] D. Vorselen *et al.*, « The fluid membrane determines mechanics of erythrocyte extracellular vesicles and is softened in hereditary spherocytosis », *Nat. Commun.*, vol. 9, n° 1, p. 4960, nov. 2018, doi: 10.1038/s41467-018-07445-x.
[35] S. Kang, J. Park, et M. Lee, « Machine learning-enabled autonomous operation for atomic force microscopes », *Rev. Sci. Instrum.*, vol. 94, n° 12, p. 123704, déc. 2023, doi: 10.1063/5.0172682.

[36] A. S. Barnard, B. Motevalli, A. J. Parker, J. M. Fischer, C. A. Feigl, et G. Opletal, « Nanoinformatics, and the big challenges for the science of small things », *Nanoscale*, vol. 11, n° 41, p. 19190–19201, 2019, doi: 10.1039/C9NR05912A.
[37] I. Sokolov, « On machine learning analysis of atomic force microscopy images for image classification, sample surface recognition », *Phys. Chem. Chem. Phys.*, vol. 26, n° 15, p. 11263–11270, 2024, doi: 10.1039/D3CP05673B.
[38] K. Ito *et al.*, « Host Cell Prediction of Exosomes Using Morphological Features on Solid Surfaces Analyzed by Machine Learning », *J. Phys. Chem. B*, vol. 122, n° 23, p. 6224–6235, juin 2018, doi: 10.1021/acs.jpcb.8b01646.

Supplementary Information

Large extracellular vesicles subsets and contents discrimination: the potential of morpho mechanical approaches at single EV level

Geetika Raizada[1], Benjamin Brunel[1], Joan Guillouzouic[3], Eric Le Ferrec[3], Eric Lesniewska [2], Wilfrid Boireau [1], Céline Elie-Caille [1]

1. Université Marie et Louis Pasteur, UFC, CNRS, Institut FEMTO-ST, F-25000 Besançon, France

2. ICB UMR 6303 CNRS, University of Bourgogne Franche-Comté, F-21078 Dijon, France

3. Univ Rennes, Inserm, EHESP, Irset (Institut de Recherche en Santé Environnement et Travail), UMR_S 1085, F-35000, Rennes, France

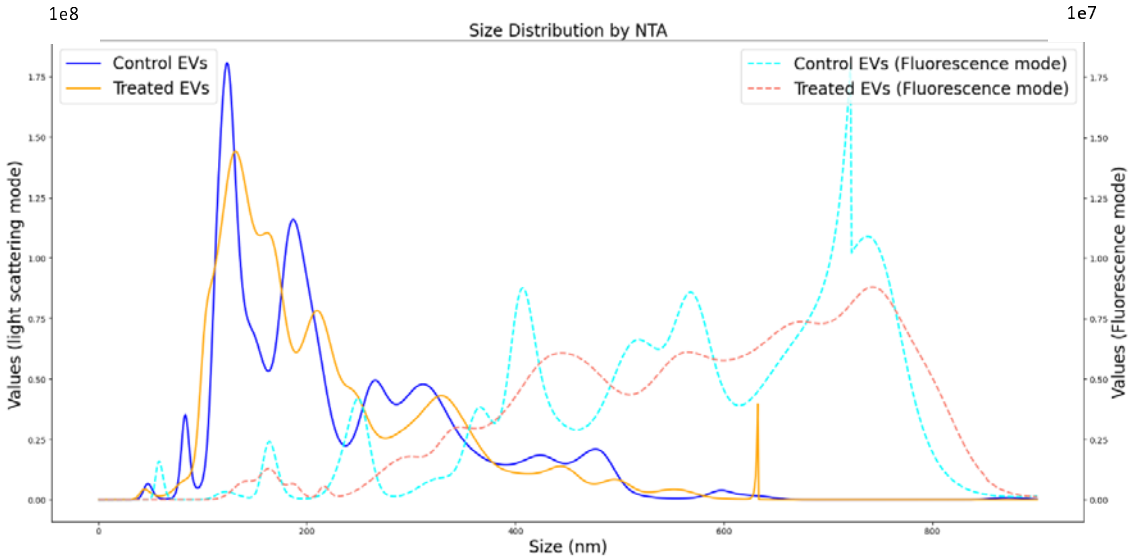

Figure S1. NTA results showing the concentration of particles as a function of their size for control and treated samples.

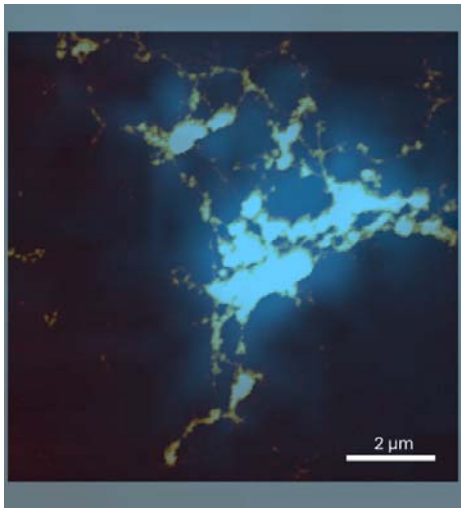

Figure S2. Overlaid fluorescence and AFM image (figure 4e). This overlaid image shows the presence of mitochondria inside these vesicles.

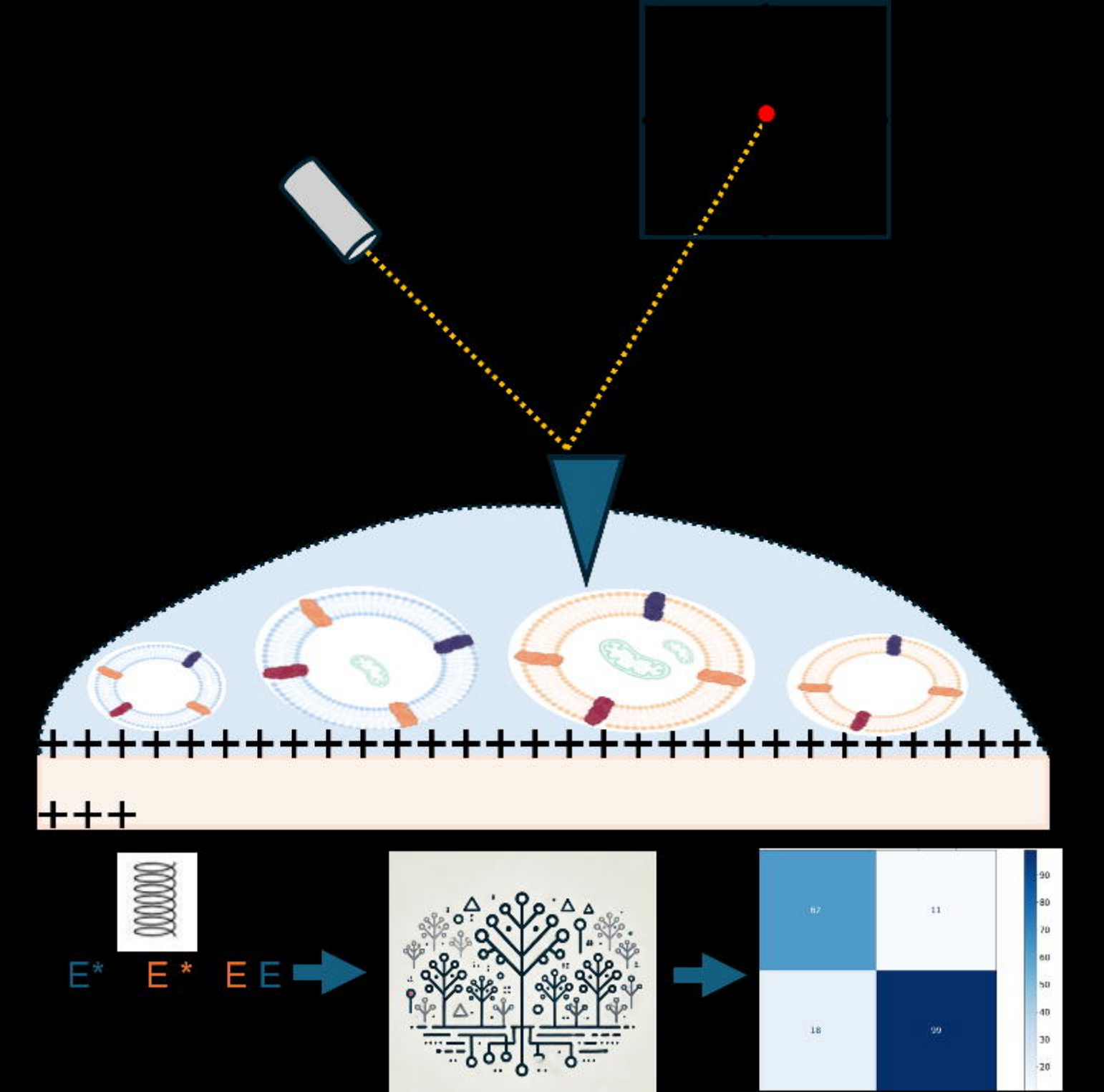
E*
E*
E E
62
11
18
99
90
80
70
60
50
40
30
20